HiSST: 3rd International Conference on
High-Speed Vehicle Science Technology
14 -19 April 2024, Busan, Korea

Rapid Design Method for Planform-customized Waveriders Based on the Second-order Curved Shock Theory

Yiqi Tang[1], Zhancang Hu[2], Xiaoting Ding[3], Xiaogang Zheng[4], Chongguang Shi[5], Yancheng You[6]

Abstract

The planform shape of waveriders is closely bound up with waveriders' geometric properties and aerodynamic characteristics. To enhance design freedom and efficiency, a rapid design methodology for planform-customized waveriders is proposed in this paper. The more general geometrical relationships between design curves are revealed, and an approximate analytical method for solving the post-shock flowfield is derived based on the second-order curved shock theory. The double-swept waverider and the delta-winged waverider are designed respectively. Numerical simulation results indicate that this method substantially enhances computational efficiency while maintaining high accuracy. The influence of angle of attack on the aerodynamic performance of the waverider is investigated by viscous numerical simulation. It is found that the lift coefficient of the waverider increases nonlinearly with the angle of attack under design conditions. This method broadens the design idea of the planform-customized waveriders and promote its engineering application.

Keywords: *Waverider, Planform-customized, Curved Shock Theory, Hyper Sonic, Rapid Design*

Nomenclature

uppercase letters
V – velocity
S_a – shock curvature in flow plane
S_b – shock curvature in flow-normal plane
P – normalized pressure gradient
D – streamline curvature
T – temperature
M – Mach number
R – gas constant
S_w – windward area
S_{ref} – reference area
Vol – volume
C_L – lift coefficient
lowercase letters
r – curvature radius
s – the length along the streamline
n – the length perpendicular to the streamline
p – pressure

Greek symbols
δ – the flow deflection angle
α – angle of attack
θ – shock angle
σ – the length of the shock
γ – specific heat ratio
ρ – density
ω – vorticity
η – volume ratio
Γ – normalized vorticity
subscripts
1 – pre-shock parameter
2 – post-shock parameter
0 – inflow parameters
t - stagnation parameter
superscripts
$'$ – gradient of variables

[1] *School of Aerospace Engineering, Xiamen University, China, 35020230156550@stu.xmu.edu.cn*
[2] *School of Aerospace Engineering, Xiamen University, China, 35020200156007@stu.xmu.edu.cn*
[3] *School of Aerospace Engineering, Xiamen University, China, 35020211151468@stu.xmu.edu.cn*
[4] *School of Aerospace Engineering, Xiamen University, China, xiaogangzheng@xmu.edu.cn (Corresponding Author)*
[5] *School of Aerospace Engineering, Xiamen University, China, chongguangshi@xmu.edu.cn*
[6] *School of Aerospace Engineering, Xiamen University, China, yancheng.you@xmu.edu.cn (Corresponding Author)*

1. Introduction

Hypersonic vehicles, with their vast operational domains, extreme speeds, long ranges, and high precision, hold significant military and civilian value [1]. However, as Mach numbers increase, conventional aerodynamic layouts for hypersonic vehicles exhibit more pronounced shock wave detachment, encountering the "lift-to-drag ratio barrier" [2]. To meet the aerodynamic requirements for high lift-to-drag ratios under hypersonic flight conditions, a waverider configuration with an attached shock wave at the leading edge, which encapsulates high-pressure airflow beneath the vehicle, has become an ideal candidate for the aerodynamic layout design of hypersonic vehicles [3-5]. In recent years, extensive and in-depth work around waverider design has been conducted worldwide [6].

The waverider concept was first introduced by Nonweiler in 1959 [7], who designed a "∧"-shaped waverider (also known as a wedge-induced waverider) based on a two-dimensional wedge flow field. Subsequently, Jones et al. designed cone-induced waveriders based on axisymmetric conical flow [8]. Moreover, more general three-dimensional flow fields have also been utilized in waverider design [9-10]. In most cases, the shock wave shape needs to be specified in advance to meet increasingly complex design requirements. Thus, a class of osculating theory for spanwise waverider design has gradually developed. In 1990, Sobieczky et al. first introduced the osculating cone design theory [11], using a series of conical flow fields within osculating planes to approximate three-dimensional supersonic flow. Sobieczky et al. later proposed an osculating axisymmetric theory [12], where the basic flow field within each osculating plane is obtained by scaling a single axisymmetric basic flow field. Building on this, Rodi further developed the osculating flow field theory [13], allowing the use of different axisymmetric basic flow fields in each osculating plane as per design requirements. Additionally, modified designs of waveriders to improve aerodynamic performance have been studied [14].

Traditional waverider designs commence with the leading-edge profile, deriving the surface through streamline tracing in the basic flow field, with the leading-edge profile typically represented as the exit section's projection. Clearly, the waverider planform shape is not freely specifiable; it is inherently tied to geometric characteristics like sweep and dihedral angles, and volumetric ratio, further impacting the waverider's aerodynamic performance [15-17]. Consequently, waverider design methods with customizable shapes have gradually become a research focus. He X first proposed a method for finned waveriders by specifying the planform shape, freestream edge shape, and compression surface trailing edge shape [18]. Similarly, Kontogiannis et al. achieved flexible construction of the osculating cone waverider geometry by parameterizing these profiles [19]. Starkey et al. studied the impact of power-law planform shapes on waverider performance within a wedge flow field [20]. Since 2011, Rodi first investigated osculating cone and osculating flow field waveriders with specific sweep angles, which could generate stable separation vortices on the upper surface to improve low-speed lift-to-drag characteristics [21-22]. While direct methodologies were not detailed, this research provided new insights into the fixed planform shape waverider designs. For instance, Zhao Z T et al. designed swept waveriders with "sharp wing" and "delta wing" configurations based on the geometric relationships of osculating cone waveriders [23]. Chen S H et al. designed an osculating cone waverider with adjustable sweep angle and dihedral angle by specifying the horizontal/bottom projection profile of the leading edge [24]. Similarly, Chen S H et al. designed an integrated waverider with a droplet-shaped intake based on the planform leading edge definition method [25]. Recently, based on the osculating cone theory, single-swept leading edge waveriders have been extended to double-swept configurations, generating stronger vortices at low speeds and further enhance aerodynamic performance [26-27].

The aforementioned design methods [19, 23-27] for fixed planform shape waveriders are limited by osculating cone theory. In contrast, osculating axisymmetric theory broadens the design horizon, accommodating more complex axisymmetric flows with curved shocks, thus offering a refined framework for waverider construction. This leads to the second issue in waverider design: the method for computing flow field parameters of the basic flow field related to the type of flow field. Traditional approaches, like the method of characteristics (MOC), demand extensive computations across the entire flow field before tracing streamlines [12, 28], hampering design optimization due to their computational intensity. Recently, Shi et al. derived a second-order curved shock theory to obtain high-order flow parameters immediately behind the shock, enabling rapid post-shock flow field solution [29]. Therefore, to address the aforementioned issue, this paper proposes the Rapid Design Method for Planform-Customized Waverider (RPCW) based on the second-order curved shock theory. The RPCW approach,

integrating Planform Profile Curve (PPC) and Shock Wave Profile Curve (SWPC), negates the need for exhaustive pre-solution of the flow field. Instead, a fast and approximate analytical method based on the second-order curved shock theory is used to quickly obtain the streamline and its parameters in each osculating plane once the leading-edge points of streamline tracing are determined.

In the following sections, the RPCW method is introduced in detail, revealing the geometric relationships between design curves. Then, two typical planform shapes are specified as inputs. Both inviscid and viscous numerical simulations are employed to validate the efficacy and applicability of this innovative waverider design method. Finally, an analysis and comparison of the aerodynamic characteristics of these two waveriders are conducted.

2. Rapid Design Method for Planform-Customized Waverider

Similar to the osculating axisymmetric theory [12], in the RPCW method, the three-dimensional post-shock supersonic flow is discretized into a series of axisymmetric flows within osculating planes. Unlike the traditional approach, the RPCW method obviates the need for employing MOC to solve the entire axisymmetric basic flow field prior to streamline tracing. Through the following three fundamental steps, a planform-customizable waverider can be obtained.

2.1. Determination of FCT: Specifying SWPC and PPC

Fig. 1 illustrates the presence of three design curves in the RPCW method: the shock wave profile curve (SWPC) within the base plane, the flow capture tube (FCT), and the planform profile curve (PPC). Specifically, the FCT and PPC are projections of the waverider leading-edge onto the base plane (yoz plane) and the horizontal plane (xoy plane), respectively. The SWPC is pre-specified due to its crucial role in shaping the three-dimensional basic flowfield. On this basis, the PPC serves as another design input to determine the waverider leading-edge. As depicted in the rear view in Fig. 1, point A (y_A, z_A) signifies the curvature center of the SWPC at shock point D (y_D, z_D). The flow within the osculating plane AD (XOY plane) is scaled from the provided axisymmetric basic flowfield, with the scaling factor determined by the curvature radius r_D at point D of the SWPC, as illustrated in Fig. 2. The flow within the osculating plane AD is projected onto the horizontal plane, as shown in the top view in Fig. 1. The shock wave A_0D intersects with the PPC at point B_0, which is the leading-edge point of the waverider within the osculating plane AD, also functioning as the starting point for streamline tracing. Correspondingly, the projection of point B0 onto the base plane is designated as point B; it lies on AD and satisfies $y_B=y_{B0}$, as depicted in the rear view in Fig. 1. By repeating this process along the SWPC, the entire FCT within the base plane can be obtained. The position (X_B, Y_B) of point B within the osculating plane AD can be ascertained based on its relative position along AD. Further, point B_0 (X_{B0}, Y_{B0}) is determined by projecting forward from point B to the shock wave A_0D.

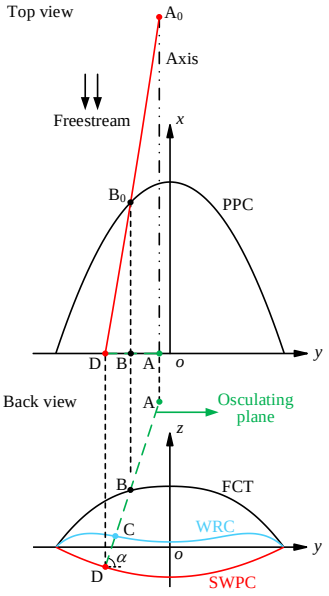

Fig 1. Geometrical relations between design curves

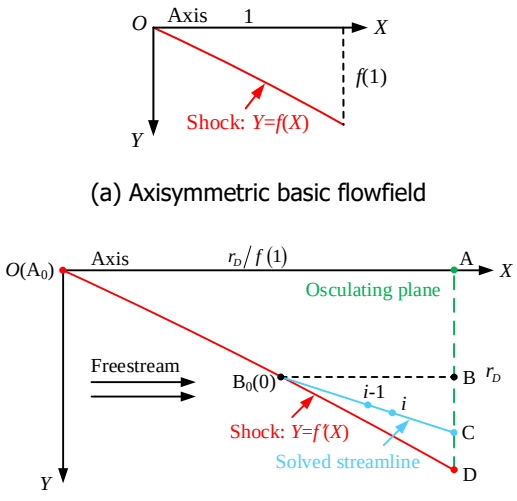

Fig 2. Schematic for flow condition

2.2. Computation of Streamline in Osculating Plane

Before introducing the approximate analytical method for flow fields, a concise overview of curved shock theory is essential. First proposed by Mölder [30], the theory defines the key characteristics of flow across a curved shock wave, as illustrated in Fig. 3(a). The incoming flow with velocity V_1 passes through the curved shock A, resulting in a post-shock flow velocity V_2. V_1 and V_2 form the flow plane B. The plane orthogonal to both A and B is defined as the flow-normal plane C. The intersection of planes C and A yields the shock line b-b. The shock line a-a within plane A intersects with shock line b-b at point c. In plane A, a Cartesian coordinate system is instituted, as illustrated in Fig. 3(b), where the angles between V_1, V_2, and the x-axis are labeled δ_1 and δ_2, correspondingly, with the flow deflection angle across the shock noted as $\delta=\delta_2-\delta_1$. Concurrently, the shock angle θ is defined as the angle between the shock line a-a and velocity V_1. The length of the shock line a-a is denoted by σ, and variables s and n denote the lengths along and perpendicular to the streamline, respectively. From these definitions, the streamwise curvature S_a of the shock can be derived using the equation $S_a=-1/R_a=\partial\theta_1/\partial\sigma$. Similarly, the curvature S_b of the shock in the flow-normal plane is computed using the equation $S_b=-1/R_b=-\cos\theta_1/y$, where y signifies the distance from the shock to the x-axis.

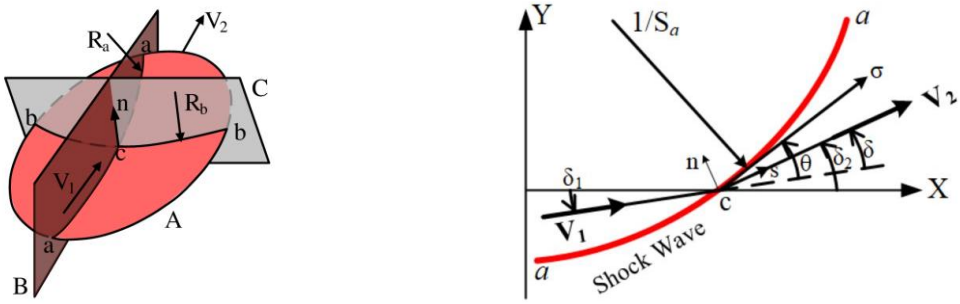

(a) Geometry of curved shock [30] (b) Variables in the flow plane [29]

Fig 3. Sketch of the curved shock theory

Mölder [30] defined the following variables:

$$\begin{aligned}&\text{normalized pressure gradient: } P=\left(\partial p/\partial s\right)\big/\rho V^2,\\&\text{streamline curvature: } D=\partial\delta/\partial s,\\&\text{normalized vorticity: } \Gamma=\omega/V,\end{aligned}\tag{3.1}$$

where p is pressure, ρ is density, and ω is vorticity. Utilizing these variables, the first-order curved shock equations become:

$$\begin{aligned}A_1P_1+B_1D_1+E_1\Gamma_1&=A_2P_2+B_2D_2+CS_a+GS_b,\\A_1'P_1+B_1'D_1+E_1'\Gamma_1&=A_2'P_2+B_2'D_2+C'S_a+G'S_b.\end{aligned}\tag{3.2}$$

with coefficients A, B, C, E, G being expressions dependent on the inflow conditions and the shock angle, detailed in Mölder's work [30]. Extending from first-order curved shock theory, Shi derived the second-order curved shock theory [29] by first defining the gradients of the variables as follows:

$$\begin{aligned}&\text{normalized second-order pressure gradient: } P'=\frac{1}{\rho V^2}\frac{\partial^2 p}{\partial s^2},\\&\text{streamline curvature gradient: } D'=\partial^2\delta/\partial s^2,\\&\text{normalized vorticity gradient: } \Gamma'=\partial\Gamma/\partial\sigma,\\&\text{shock curvature gradient: } S_a'=\partial S_a/\partial\sigma,\quad S_b'=\partial S_b/\partial\sigma.\end{aligned}\tag{3.3}$$

Using these variables, the second-order curved shock equations are formulated as:

$$\begin{aligned}A_1''P_1'+B_1''D_1'+E_1''\Gamma_1'&=A_2''P_2'+B_2''D_2'+C''S_a'+G''S_b'+\text{const.}'',\\A_1'''P_1'+B_1'''D_1'+E_1'''\Gamma_1'&=A_2'''P_2'+B_2'''D_2'+C'''S_a'+G'''S_b'+\text{const.}'''.\end{aligned}\tag{3.4}$$

The coefficients in this set of equations are likewise functions of the inflow conditions and the shock angle, albeit of greater complexity, as thoroughly described in Shi's work [29].

Though the second-order curved shock equations are applicable only near the shock, the precise high-order derivatives of aerodynamic parameters immediately behind the shock can indicate the direction and trend of parameter changes. By utilizing the known aerodynamic parameters and their derivatives at a shock point and employing a Taylor series expansion, a polynomial that approximates parameter distribution along the streamline can be formed. Shi's work [29] reveals that for various shocks—conical, planar curved, and axisymmetric curved—the pressure gradient (P) and streamline curvature (D) vary markedly along the streamline, yet the second-order pressure gradient (P') and the streamline curvature gradient (D') tend to remain stable. Compared to MOC outcomes, the second-order curved shock equations effectively estimate the post-shock flow field for planar and axisymmetric curved shocks.

Then, the approximate analytical method based on the second-order curved shock theory is utilized to quickly obtain the streamline and associated flow parameters within each osculating plane. Using the shock point B_0 in Fig. 2 (b) as an example, the flow parameters (such as the pressure p_{B0} and flow deflection angle δ_{B0}) immediately behind the shock wave, along with their first-order derivatives (such as the pressure gradient P_{B0} and streamline curvature D_{B0}) and second-order derivatives (such as the second-order pressure gradient P'_{B0} and streamline curvature gradient D'_{B0}), can be respectively determined based on the oblique shock wave relations, the first-order and second-order curved shock equations, under known incoming flow conditions. Although the curved shock theory focuses on flow structures in the close vicinity of shock waves, the precise higher-order derivatives of flow parameters illustrate the direction and trend of parameter changes. Hence, according to the assumption that P'_{B0} and D'_{B0} are constants along the streamline, the coordinates and other flow parameters of the unsolved point i on the streamline B_0C can then be evaluated as follows by using Taylor series:

$$\begin{aligned} y_i &= y_{i-1} + dx\frac{dy}{dx} + \frac{(dx)^2}{2}\frac{d^2y}{dx^2} + \frac{(dx)^3}{6}\frac{d^3y}{dx^3} + \ldots, \\ \delta_i &= \delta_{i-1} + ds\frac{d\delta}{ds} + \frac{(ds)^2}{2}\frac{d^2\delta}{d\mathrm{s}^2} + \ldots, \\ p_i &= p_{i-1} + ds\frac{dp}{ds} + \frac{(ds)^2}{2}\frac{d^2p}{d\mathrm{s}^2} + \ldots, \end{aligned} \tag{3.5}$$

where

$$\begin{aligned} &\frac{dy}{dx} = \tan\delta_{i-1}, \quad \frac{d^2y}{dx^2} = \frac{D_{i-1}}{\cos^3\delta_{i-1}}, \quad \frac{d^3y}{dx^3} = \frac{3D_{i-1}^2\tan\delta_{i-1} + D'_{B0}}{\cos^4\delta_{i-1}}, \\ &\frac{d\delta}{ds} = \frac{\partial\delta}{\partial s} = D_{i-1}, \quad \frac{d^2\delta}{d\mathrm{s}^2} = \frac{\partial^2\delta}{\partial\mathrm{s}^2} = D_{B0}, \\ &\frac{dp}{ds} = \frac{\partial p}{\partial s} = \rho_{i-1}{V_{i-1}}^2 P_{i-1}, \quad \frac{d^2p}{d\mathrm{s}^2} = \frac{\partial^2 p}{\partial\mathrm{s}^2} = \rho_{i-1}{V_{i-1}}^2 P'_{B0}. \end{aligned} \tag{3.6}$$

Since the total pressure p_t and total temperature T_t remain constant along the streamline, we have:

$$\begin{aligned} p_t &= p_i\left(1 + \frac{\gamma-1}{2}M_i^2\right)^{\gamma/(\gamma-1)} = p_0\left(1 + \frac{\gamma-1}{2}M_0^2\right)^{\gamma/(\gamma-1)}, \\ T_t &= T_i\left(1 + \frac{\gamma-1}{2}M_i^2\right) = T_0\left(1 + \frac{\gamma-1}{2}M_0^2\right). \end{aligned} \tag{3.7}$$

The density ρ and velocity V can then be determined using the equation:

$$\rho_i = \frac{p_i}{RT_i}, \quad V_i = M_i a_i = M_i\sqrt{\gamma RT_i}. \tag{3.8}$$

The streamline curvature D and the pressure gradient P can be solved using Equation (1.3):

$$P_i = P_{i-1} + P'_{B0}ds, \quad D_i = D_{i-1} + D'_{B0}ds. \tag{3.9}$$

Thus, as shown in Fig. 2(b), once the shock wave A_0D and leading-edge point B_0 within the osculating plane are determined, the above process can be repeated to complete the solution of the streamline

B_0C and associated flow parameters. B_0C is the waverider surface profile within this osculating plane. Combining the streamline within each osculating plane forms the complete waverider lower surface, with its exit profile curve as shown by the WRC in Fig. 1. In addition, the freestream surface (aligned to the freestream direction) is selected as the waverider upper surface, whose exit profile curve matches precisely with the FCT in Fig. 1.

2.3. Prediction of geometric and inviscid aerodynamic performance

Using the RPCW method, the pressure distribution on the waverider's surfaces is determinable, allowing for the computation of its lift and drag. Fig. 4(a) illustrates the process of evaluating the forces acting on the waverider lower surface. The pressure at each grid point is obtainable as described in Section 2.2. Integrating the pressure exerted on each quadrilateral micro-element yields the force on the surface. For instance, for the quadrilateral micro-element ABCD, its windward area S_w can be calculated using the following vector relationship:

$$S_w = \frac{1}{2}\left|\bar{n}\right| = \frac{1}{2}\left|\overline{AC} \times \overline{DB}\right|, \tag{3.10}$$

where the magnitude of vector n represents the micro-element's area, and its direction represents the normal to the micro-element's surface. Subsequently, the force acting on this micro-element can be calculated using the average pressure at its four vertices as follows:

$$p_{avg} = \frac{p_A + p_B + p_C + p_D}{4}, \quad F = p_{avg} \times S_w. \tag{3.11}$$

This allows for the determination of the lift and drag forces (at a 0-degree angle of attack) acting on this micro-element as expressed by:

$$L = F\frac{\bar{n}_z}{\left|\bar{n}\right|} = p_{avg}S_w\frac{\bar{n}_z}{\left|\bar{n}\right|}, \quad D = F\frac{\bar{n}_x}{\left|\bar{n}\right|} = p_{avg}S_w\frac{\bar{n}_x}{\left|\bar{n}\right|}. \tag{3.12}$$

By integrating the lift and drag forces across all micro-elements on the lower surface, the total forces acting on the waverider's lower surface are ascertainable. For the upper surface, treated as a free stream surface parallel to the inflow, the pressure uniformly matches the free stream pressure. The method for calculating forces on the upper surface mirrors that of the lower and is not repeated. Hence, the aggregate of lift and drag across both surfaces constitutes the waverider's total lift L_{all} and drag D_{all}, with the lift-to-drag ratio given by L_{all}/D_{all}.

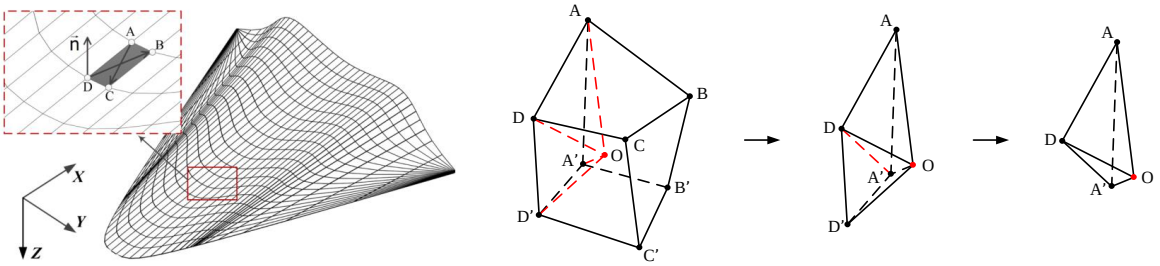

(a) force and area of lower surface [31] (b) volume of the waverider

Fig 4. Schematic of prediction method for geometric and inviscid aerodynamic performance

The reference area S_{ref} is defined as the waverider's horizontal projection area S_p, calculated by:

$$S_{ref} = S_p = \int S_w \left|\frac{\bar{n}_z}{\bar{n}}\right|. \tag{3.13}$$

The volumetric efficiency η of the waverider can be quickly estimated using the equation:

$$\eta = \frac{Vol^{2/3}}{S_{ref}}, \tag{3.14}$$

where Vol denotes the waverider's volume, estimated as follows. As shown in Fig. 4(b), consider a

hexahedral micro-element ABCD-A′B′C′D′ within the waverider, with points A, B, C, D are on the lower surface, and A′, B′, C′, D′ on the upper. Initially, the center point O of the micro-element is determined by averaging the eight vertices. The micro-element is then segmented into six smaller volumes, like O-AA′D′D. Subsequently, these are split into even smaller volumes, e.g., O-AA′D. The volume of such a tetrahedron is calculable through the vector triple product:

$$Vol_{\text{O-AA'D}} = \left|\left(\overline{OA}\times\overline{OA'}\right)\cdot\overline{OD}\right|/6. \tag{3.15}$$

By determining the volume of the 12 tetrahedra resulting from the micro-element's division and aggregating these volumes, the volume of micro-element ABCD-A′B′C′D′ is ascertainable, facilitating the calculation of the waverider's overall volume via integration.

3. Application of Rapid Design Method for Planform-Customized Waverider

All CFD results presented in this paper are obtained using ANSYS Fluent, employing a density-based solver. The flow is assumed to be an ideal gas with a constant specific heat ratio γ=1.4. For inviscid simulations, Euler equations are discretized and integrated using the finite volume method, with inviscid fluxes calculated using a second-order AUSM upwind scheme. For viscous simulations, the three-dimensional Navier-Stokes equations are discretized in space using the finite volume method, and the k-ω SST turbulence model is used for closure. Both convective and viscous fluxes are calculated using a second-order AUSM upwind scheme. The molecular viscosity is calculated using Sutherland's formula to ensure computational accuracy and stability for strong shock calculations. Boundary conditions include a slip adiabatic wall for the waverider surface, a pressure far-field condition for the domain inlet, and a pressure outlet condition for the domain exit.

3.1. Numerical Validation of the Design Method

To assess the RPCW's efficacy, various PPCs are employed to generate waveriders of distinct planform shapes. For instance, the delta wing waverider's design curves are shown in Fig. 5. The design altitude is set at 30km, with an incoming Mach number of 8. The specific heat ratio is assumed to be a constant value of 1.4. The curved shock wave profile within the axisymmetric basic flowfield is specified by $Y=0.03X^2+0.18X$.

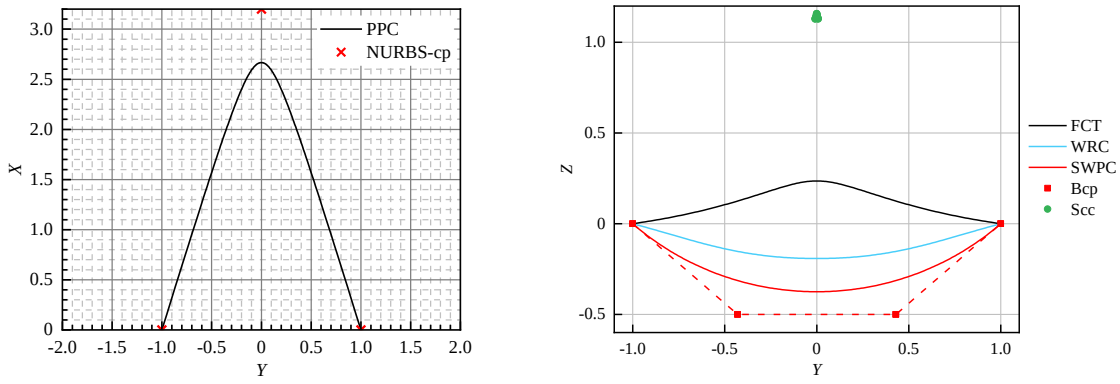

(a) Horizontal projection view (b) Base plane view

Fig 5. Design curves of the delta wing waverider

Pressure contours on the waverider's lower surface and outlet under inviscid conditions are depicted in Fig. 6(a) and Fig. 6(c), respectively. It is seen that the waverider generated using the RPCW method demonstrates commendable wave-riding characteristics, with no leading-edge airflow leakage. The shock waves observed in the CFD outcomes align with the theoretically predefined shock waves. Figs. 6(b) and Fig. 6(d) illustrate the pressure contours under viscous conditions, where slight airflow leakage is observed at the leading edge due to viscosity, and the theoretical shock wave marginally surpasses the CFD results. Nevertheless, the curved shock consistently remains attached to the waverider's lower surface, affirming that the waverider achieved through the inviscid design method in this study maintains robust wave-riding characteristics even under viscous conditions.

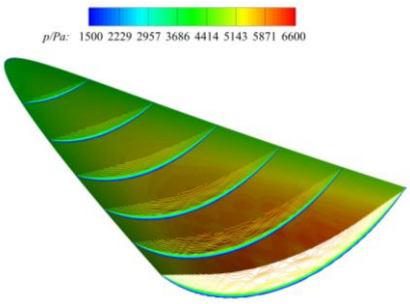

(a) Pressure contour of the lower surface (inviscid)

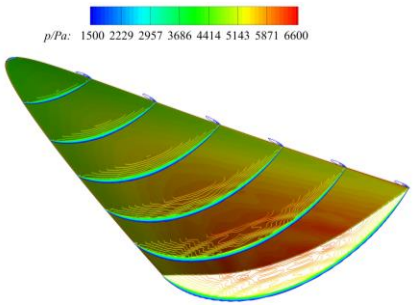

(a) Pressure contour of the lower surface (viscous)

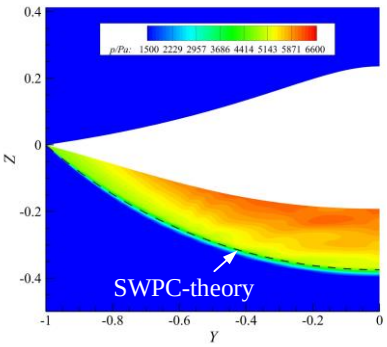

(c) Pressure contour of the outlet section (inviscid)

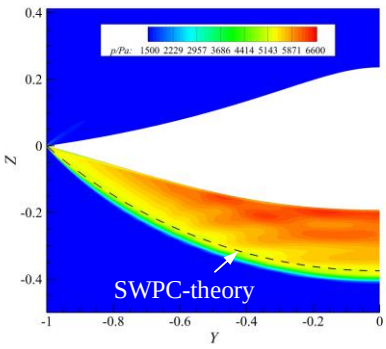

(d) Pressure contour of the outlet section (viscous)

Fig 6. Pressure contours of the delta wing waverider from different views

Table 1. Comparison of geometric properties and aerodynamic characteristics

Waverider type	L/D(theory)	L/D(CFD)	ε(%)	η(theory)	η(CFD)	ε(%)
double-swept	4.5428	4.4881	1.2188	0.1841	0.1842	0.0543
delta wing	4.9528	4.8609	1.8906	0.18905	0.18907	0.01058

Table 1 compares the theoretical and CFD-derived lift-to-drag ratios (L/D) and volumetric efficiencies (η) of waveriders, showing strong agreement with theoretical predictions within a 2% error margin for L/D and less than 0.1% for η in inviscid conditions. In addition, due to the use of the approximate analytical method for individual streamline calculations before tracing, as opposed to the grid-based whole flowfield solution with MOC, the computation time has been significantly reduced. For instance, the RPCW method designs a double swept waverider in just 1.45 seconds, whereas the MOC method takes 29.38 seconds, making RPCW 20 times faster.

3.2. Aerodynamic Characteristics Analysis of Waveriders at Design Conditions

Additionally, the aerodynamic characteristics of the double-swept waverider and delta wing waverider designed using the RPCW method are investigated through numerical simulations at various angles of attack (AOA). Results reveal that the lift-to-drag ratio L/D decreases for both waverider types as the AOA increases (see Fig. 7 (a)). Conversely, the lift coefficient C_L demonstrates a nonlinear increase with the AOA (see Fig. 7 (b)). This phenomenon has been noted in previous studies [32-36]. Liu Chuanzhen [35] and Li Jun [36] suggested that the "wave effect" on the waverider lower surface is the primary contributor to this nonlinear increase. To validate this hypothesis, this section first analyzes the contribution of the lift coefficients CL from the upper and lower surfaces of the two types of waveriders and compares them with their respective linear trends.

By separately counting the lift coefficients provided by the upper and lower surfaces, it can be found that for both types of waveriders, the lower surface contributes significantly more than the upper surface, and shows a non-linear growth trend that similar to the overall lift coefficient of the waverider (see Fig. 7 (c) and Fig.7 (d)). For instance, for the double-swept waverider at α=20°, the lower surface

accounts for 98.41% of the lift, while the upper surface contributes a mere 1.59%. With increasing AOA, the slope of the C_L curve for the lower surface of the double-swept waverider shows a progressive, non-linear rise starting from α>4°, contrasting with the upper surface's C_L curve, which flattens and then declines past α>8°. This pattern strongly suggests that the non-linear lift enhancement at high AOAs in hypersonic conditions is predominantly influenced by the lower surface.

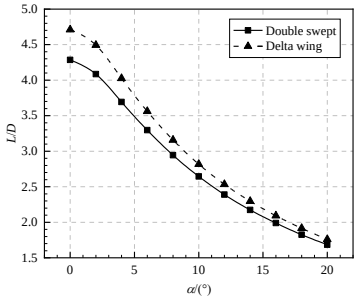

(a) lift-to-drag ratio (L/D)

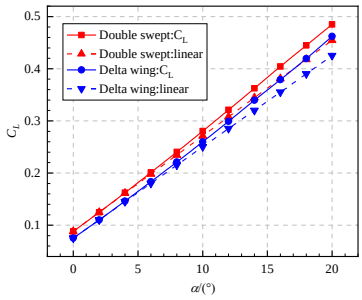

(b) lift coefficient (C_L)

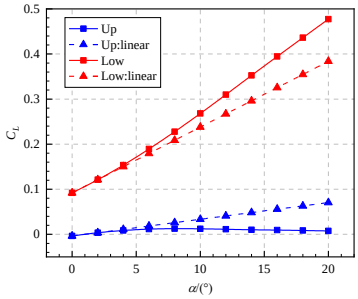

(c) The lift coefficient of the upper and lower surfaces of the double swept waverider

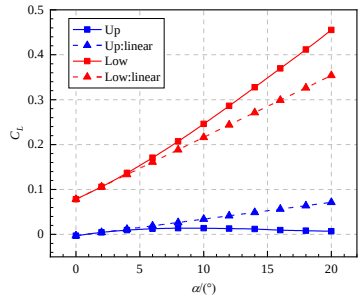

(d) The lift coefficient of the upper and lower surfaces of the delta wing waverider

Fig 7. The variation of aerodynamic characteristics of waveriders with angle of attack

To elucidate the "wave effect" on the aerodynamics of waverider lower surface, Fig. 8(a) presents the pressure contours on the lower surfaces of the double-swept waverider and delta wing waverider at α=0°, α=10°, and α=20°. It is evident that with increasing AOA, the high-pressure regions on the lower surfaces of both waverider types migrate from the inboard rear towards the outboard leading edge. Fig.8(b) displays the sectional pressure distributions for both waverider types at α=0°, α=10°, and α=20°. Despite the varying extents of leading-edge shock wave detachment due to increased AOA, the overall high-pressure air leakage remains minimal. Liu Chuanzhen pointed out that with attached shocks, the lower surface's post-shock pressure and, consequently, the lift coefficient rise nonlinearly with AOA [35]. Contrarily, Li Jun observed that waveriders experiencing minor shock detachment showed less pronounced nonlinear lift enhancements [36]. Thus, the mechanism of nonlinear lift augmentation in hypersonic waveriders at high AOAs merit further exploration.

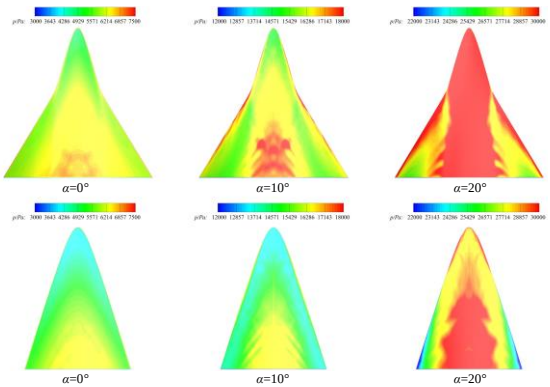

(a) on the low surface

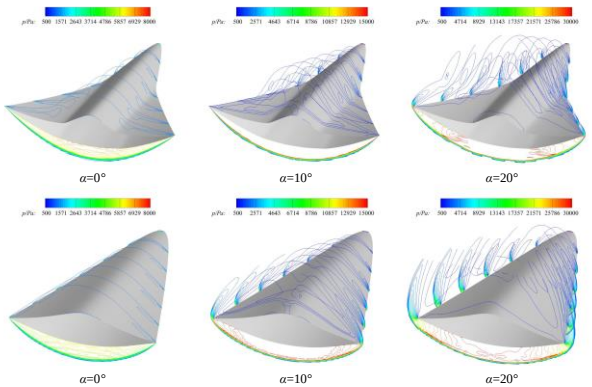

(b) on the Cross-section

Fig 8. Pressure distribution of the waverider under design condition

4. Conclusion

In this paper, a rapid design method for planform-customized waveriders (RPCW) based on the second-order curved shock theory is presented and validated through numerical simulations. Waveriders designed using the RPCW method exhibit good wave-riding characteristics in inviscid conditions. The RPCW method achieves a 20-fold increase in computational efficiency over traditional MOC-based techniques, with lift-to-drag and volumetric efficiency discrepancies kept below 2% and 0.06%, respectively. In viscous scenarios, minor flow spillage occurs at the leading edge, yet the three-dimensional curved shock wave predominantly adheres to the lower surface. As the angle of attack escalates in high-speed conditions, the lift-to-drag ratio monotonically decreases, whereas the lift coefficient shows nonlinear growth. Notably, the lower surface contributes more substantially to the lift coefficient than the upper surface, with the "wave effect" on the lower surface being pivotal for the nonlinear lift enhancement at steep angles. The RPCW method broadens the conceptual framework for planform-customized waveriders and promote its engineering application. Future work will focus on further optimization of waverider design and the study of their aerodynamic performance.

References

1. Bertin J J, Cummings R M. Fifty years of hypersonics: where we've been, where we're going [J]. Progress in Aerospace Sciences, 2003, 39(6–7): 511–536.
2. Kuechemann D. The aerodynamic design of air-craft[G]//Pergamon Press, 1978: 448–510.
3. Voland R T, Huebner L D, Mcclinton C R. X-43A hy-personic vehicle technology development [J]. Acta As-tronautica, 2006, 59: 181-191.
4. Walker S, Sherk J, Shell D, et al. The DARPA/AF Fal-con program: The hypersonic technology vehicle #2 (HTV-2) flight demonstration phase [C]. The 15th AIAA International Space Planes and Hypersonic Systems and Technologies Conference, 2008.
5. Mutzman R, Murphy S. X-51 development: A chief en-gineer' s perspective [C]. 17th AIAA International Space Planes and Hypersonic Systems and Technologies Con-ference, 2011.
6. D. Lunan. Waverider, a revised chronology [R]. AIAA Paper 2015-3529, 2015.
7. Nonweiler T R F. Aerodynamic problems of manned space vehicles[J]. The Journal of the Royal Aeronautical Society, 1959, 63(585): 521–528.
8. Jones J G, Moore K C, Pike J, et al. A method for de-signing lifting configurations for high supersonic speeds, using axisymmetric flow fields[J]. Archive of Applied Mechanics, 37(1): 56–72.
9. Rasmussen M L. Waverider configurations derived from inclined circular and elliptic cones[J]. Journal of Space-craft and Rockets, 1980, 17(6): 537–545.
10. Takashima N, Lewis M. Waverider configurations based on non-axisymmetric flow fields for engine-airframe in-tegration[C]//32nd Aerospace Sciences Meeting and Ex-hibit. Reston, Virigina: American Institute of Aeronautics and Astronautics, 1994.
11. H. Sobieczky, F.C. Dougherty, K. Jones. Hypersonic waverider design from given shock waves [C]. First In-ternational Waverider Symposium, University of Mary-land, College Park, 1990.
12. Sobieczky H, Zores B, Zhuo. W, et al. High speed flow design using osculating axisymmetric flows[C]//Picast. Xi'an: 1997: 1–6.
13. P.E. Rodi. The osculating flowfield method of waverider geometry generation [R].AIAA Paper 2005-511, 2005.
14. Ding F, Liu J, Shen C, et al. An overview of waverider design concept in airframe/inlet integration methodology for air-breathing hypersonic vehicles[J]. Acta Astronauti-ca, Elsevier Ltd, 2018, 152(6): 639–656.
15. Miller D S, Wood R M. Leeside flows over delta wings at supersonic speeds[J]. Journal of Aircraft, 1984, 21(9): 680-686.

16. Cockrell, s E, Jr C, et al. Aerodynamic performance and flow-field characteristics of two waverider-derived hy-personic cruise configurations[C]//33rd Aerospace Sci-ences Meeting and Exhibit. 1995: 736.

17. Strohmeyer D, Eggers T, Heinze W, et al. Planform ef-fects on the aerodynamics of waveriders for TSTO mis-sions[C]//Space Plane and Hypersonic Systems and Technology Conference. 1996: 4544.

18. He X, Rasmussen M L, Cox R A. Waveriders with fin-lets[J]. Journal of Aircraft, 1994, 31(5): 1135-1142.

19. Kontogiannis K, Sóbester A, Taylor N. Efficient parame-terization of waverider geometries [J]. Journal of Aircraft, 2016, 54 (3): 890-901.

20. Starkey R P, Lewis M J. Analytical off-design lift-to-drag-ratio analysis for hypersonic waveriders[J]. Journal of Spacecraft and Rockets, 2000, 37(5): 684-691.

21. P.E. Rodi. Geometrical relationships for osculating cones and osculating flowfield waveriders [R]. AIAA Paper 2011-1188, 2011.

22. Rodi P. Vortex lift waverider configurations[C]//50th AIAA Aerospace Sciences Meeting Including The New Horizons Forum And Aerospace Exposition. 2012: 1238.

23. Zhao Z, Huang W, Yan B, et al. Design and high speed aerodynamic performance analysis of vortex lift waverid-er with a wide-speed range[J]. Acta Astronautica, Else-vier Ltd, 2018, 151(2018): 848–863.

24. Chen S, Liu J, Huang W, et al. Design methodology of an osculating cone waverider with adjustable sweep and dihedral angles[J]. Journal of Zhejiang University-SCIENCE A, 2020, 21(9): 770-782.

25. Chen S H, Liu J, Ding F, et al. Novel design methodolo-gy of integrated waverider with drip-like intake based on planform leading-edge definition method[J]. Acta Astro-nautica, 2020, 167: 314-330.

26. Wang J, Liu C, Bai P, et al. Design methodology of the waverider with a controllable planar shape[J]. Acta As-tronautica, Elsevier Ltd, 2018, 151(February): 504–510.

27. Liu C, Liu Q, Bai P, et al. Planform-customized waverid-er design integrating with vortex effect[J]. Aerospace Science and Technology, Elsevier Masson SAS, 2019, 86: 438–443

28. J.D. Anderson. Hypersonic and High Temperature Gas Dynamics Second Edition [M]. Reston, Virginia: AIAA, Inc., 2006: 111-146, 183-257, 375-395, 415-445.

29. Shi Chongguang, Han Weiqiang, Deiterding Ralf, et al. Second-order curved shock theory [J]. Journal of Fluid Mechanics, 2020, 891: A21.

30. Mölder S. Curved shock theory[J]. Shock Waves, 2015, 26 (4): 1–17.

31. ZHENG, X.G., HU, Z.C., LI, Y.Q., ZHU, et al. 2020 Local-turning osculating cones method for waverider de-sign[J]. AIAA J. 58, 1–15.

32. LIU C Z, BAI P, CHEN BY. Design and property advantages analysis of double swept waverider [J]. Acta Aeronauti-caet Astronautica Sinica, 2017, 38 (6): 120808 (in Chi-nese).

33. WANGJ F, LIU CZ, BAIP, et al. Design methodology of the waverider with a controllable planar shape [J]. Acta Astronautica, 2018, 151 : 504-510.

34. LIU C Z, LIU Q, BAI P, et al. Planform-customized waverider design integrating with vortex effect [J]. Aero-space Science and Technology, 2019, 86 : 438-443.

35. LIUCZ, TIANJW, BAIP, et al. Nonlinear lift in-crease of double swept waverider [J]. Acta Aeronauticaet Astronautica Sinica, 2019, 40(10): 122864 (in Chinese).

36. LIJ, YIHX, WANGD, et al. Aerodynamic performance of double swept waverider based on projection method [J]. Acta Aeronauticaet Astronautica Sinica, 2021, 42(12): 124703 (in Chinese). doi: 10.7527/S1000-6893. 2021.24703